

Reconciling *Planck* cluster counts and cosmology? *Chandra*/*XMM* instrumental calibration and hydrostatic mass bias

Holger Israel^{1,*}, Gerrit Schellenberger², Jukka Nevalainen³,
Richard Massey¹, and Thomas H. Reiprich²

¹*Institute for Computational Cosmology, Department of Physics, Durham University, South Road, Durham DH1 3LE, UK*

²*Argelander-Institut für Astronomie, Auf dem Hügel 71, 53121 Bonn, Germany*

³*Tartu Observatory, 61602 Toravere, Estonia*

**E-mail: holger.israel@durham.ac.uk*

23 May 2022

ABSTRACT

The mass of galaxy clusters can be inferred from the temperature of their X-ray emitting gas, T_X . Their masses may be underestimated if it is assumed that the gas is in hydrostatic equilibrium, by an amount $b^{\text{hyd}} \sim (20 \pm 10)\%$ suggested by simulations. We have previously found consistency between a sample of observed *Chandra* X-ray masses and independent weak lensing measurements. Unfortunately, uncertainties in the instrumental calibration of *Chandra* and *XMM-Newton* observatories mean that they measure different temperatures for the same gas. In this paper, we translate that relative instrumental bias into mass bias, and infer that *XMM-Newton* masses of $\sim 10^{14} M_\odot$ ($\gtrsim 5 \cdot 10^{14} M_\odot$) clusters are unbiased ($\sim 35\%$ lower) compared to WL masses. For massive clusters, *Chandra*'s calibration may thus be more accurate. The opposite appears to be true at the low mass end. We observe the mass bias to increase with cluster mass, but presence of Eddington bias precludes firm conclusions at this stage. Nevertheless, the systematic *Chandra* – *XMM-Newton* difference is important because *Planck*'s detections of massive clusters via the Sunyaev-Zeldovich (SZ) effect are calibrated via *XMM-Newton* observations. The number of detected SZ clusters are inconsistent with *Planck*'s cosmological measurements of the primary Cosmic Microwave Background (CMB). Given the *Planck* cluster masses, if an (unlikely) uncorrected $\sim 20\%$ calibration bias existed, this tension would be eased, but not resolved.

Key words: Galaxies: clusters: general – Cosmology: observations – Gravitational lensing – X-rays: galaxies: clusters

1 INTRODUCTION

The number of Sunyaev-Zeldovich (SZ) clusters detected with *Planck* above a certain mass threshold (Planck Collaboration et al. 2013c, P13XX) falls short of the tally expected from the *Planck* primary cosmic microwave background (CMB) constraints on cosmology (Planck Collaboration et al. 2013b, P13XVI). Several possible explanations have been brought forward, such as incorrect assumptions about the cluster mass function (P13XX) or modified cosmologies including massive neutrinos and a shift in the Hubble parameter (e.g., P13XX, Hamann & Hasenkamp 2013; Battye & Moss 2014; Mantz et al. 2014; Costanzi et al. 2014). Another hypothesis is that hydrostatic cluster masses, inferred from X-ray observations of the intra-cluster medium (ICM), yielded only $\sim 60\%$ of the true cluster mass. Hydro-

dynamic cluster simulations commonly find the hydrostatic assumption to retrieve only $\sim 70\text{--}90\%$ of the true cluster mass, i.e. $M^{\text{HE}} = (1 - b_{\text{lin}}^{\text{hyd}}) M^{\text{true}}$ with a hydrostatic mass bias $b_{\text{lin}}^{\text{hyd}} = 0.1\text{--}0.3$ (e.g., Nagai, Kravtsov & Vikhlinin 2007; Laganá, de Souza & Keller 2010; Kay et al. 2012; Rasia et al. 2012; Le Brun et al. 2014; Schaye et al. 2014).

The validity of the assumption of hydrostatic equilibrium can potentially be addressed by comparing to weak gravitational lensing (WL) mass measurements, which are independent and free from assumptions of the state of the gas. Noticing a considerable overlap between the *XMM-Newton* sample of P13XX and the *Weighing the Giants* WL survey (von der Linden et al. 2014a; Kelly et al. 2014; Applegate et al. 2014), von der Linden et al. (2014b, vdL14) measured $\langle M^{\text{Pl}}/M^{\text{wl}} \rangle = 0.688 \pm 0.072$ for the most massive ($> 6 \cdot 10^{14} M_\odot$) clusters. If interpreted as a hydrostatic mass

bias, this value $b_{\text{lin}} \approx 0.3$ falls short of the $b_{\text{lin}} \approx 0.4$ necessary to reconcile P13XX with P13XVI, confirming the *Planck* cluster mass discrepancy.

Conversely, Israel et al. (2014, I14) found no significant mass bias when comparing WL estimates to *Chandra*-based hydrostatic masses. For high-mass clusters ($10^{14.5} \text{ M}_{\odot} < M_{500}^{\text{wl}} < 10^{15} \text{ M}_{\odot}$), the bias $b_{\text{log}} = -0.10_{-0.15}^{+0.17}$, is consistent with the expectation based on simulations, although with large uncertainties due to small number statistics.

An alternative hypothesis is that at least one of the two X-ray observatories is imperfectly calibrated. Indeed, difficulties modelling their (energy-dependent) effective collecting area (Grant et al. 2013) lead to uncertainty in measurements of the ICM temperature, T_X . Direct comparisons have shown that *Chandra* measures significantly higher T_X than *XMM-Newton* for the same clusters (e.g. Nevalainen, David & Guainazzi 2010), and that significant differences even exist between the *XMM-Newton* instruments (Schellenberger et al. 2014, S14). S14 propagated this difference to a change in the inferred cosmological matter density Ω_m and power spectrum normalisation σ_8 . They concluded that the temperature calibration alone is insufficient to explain the discrepancy between P13XVI and P13XX.

In this paper, we simultaneously examine the hydrostatic bias and *XMM-Newton/Chandra* instrument calibration, aiming to find a solution for the cosmological discrepancy. We extend S14 by comparing measurements in an X-ray-selected cluster sample with independent WL masses. In Section 2, we re-evaluate I14's measurements of the mass bias between *Chandra* hydrostatic and WL masses, and emulate *XMM-Newton* results based on S14's cross-calibration. Noting that the P13XX calibration relies on *XMM-Newton*, in Section 3, we assess the degree to which X-ray temperature calibration could be responsible for the P13XVI–P13XX discrepancy. We conclude in Section 4.

2 RECALIBRATING THE 400d SURVEY TO XMM-NEWTON TEMPERATURES

2.1 Hydrostatic mass bias from the 400d cluster cosmology survey

I14 recently compared WL masses to *Chandra*-based X-ray mass estimates for eight clusters drawn from the 400d cosmology cluster sample. The 400d cosmology sample selects X-ray luminous clusters at $0.35 < z < 0.90$ from the serendipitous 400d *Rosat* cluster catalogue (Burenin et al. 2007). *Chandra* data for these clusters were subsequently employed to constrain cosmological parameters via the cluster mass function (Vikhlinin et al. 2009a,b). The 400d WL survey follows up the cosmology cluster sample, in order to test the mass calibration of V09a,b with independent mass estimates. The methodology and first results of the ongoing 400d WL survey were reported in Israel et al. (2010, 2012). We refer the interested reader to these papers for details. Weak lensing masses used in this paper make use of the Bhattacharya et al. (2013) mass–concentration relation.

Hydrostatic masses in I14 were derived from the V09a *Chandra* ICM density profiles ρ_g using the Vikhlinin et al. (2006) parametrisation, and temperatures $T_X(r) = T_{\text{CXO}}(r)$. The empirical Reiprich et al. (2013) relation was used to derive a temperature profile

$$T_X(r) = T_X (1.19 - 0.84r/r_{200}) \quad (1)$$

from a cluster-averaged value T_X and I14 WL radius r_{200} . This relation was determined and can be used in the range $0.3 r_{200} < r < 1.15 r_{200}$. We then compute

$$M^{\text{HE}}(r) = \frac{-k_B T_X(r) r}{\mu m_p G} \left(\frac{d \ln \rho_g(r)}{d \ln r} + \frac{d \ln T_X(r)}{d \ln r} \right), \quad (2)$$

with k_B the Boltzmann constant, $\mu = 0.5954$ the mean molecular mass of the ICM, m_p the proton mass, and G the gravitational constant. The resulting cumulative mass profile was evaluated at r_{500} taken from WL. Uncertainties on T_{CXO} and r_{500}^{wl} were propagated into an uncertainty on $M_{500}^{\text{hyd}}(r_{500}^{\text{wl}})$.

2.2 Monte Carlo analysis

We adopt a Monte Carlo approach to derive hydrostatic masses. In our scheme, the V09a cluster-averaged temperature T_{CXO} , the square of the Israel et al. (2012, I12) WL cluster radius $(r_{500}^{\text{WL}})^2$, and the slope, normalisation, and intrinsic scatter of the S14 *Chandra* \leftrightarrow *XMM-Newton* calibration relation are sampled from their Gaussian distributed probability densities. We point out that we model each of our clusters independently. By choosing $(r_{500}^{\text{WL}})^2$, whose I12 measurements we empirically find to follow a normal distribution, we are able to easily reproduce the asymmetric uncertainties in r_{500} , improving our treatment from I14. Using 10^6 Monte Carlo realisations, we excellently recover the I12 WL masses. Through the use of r_{500}^{WL} in Eq. (1), the updated account of its asymmetric uncertainties results in slightly lower *Chandra* hydrostatic masses. Compared to I14, *Chandra* hydrostatic masses are lower by an average $(1.2 \pm 0.3) \%$ (compare Table 1 to Table 2 of I14). Our new Monte Carlo technique leads to smaller uncertainties in the hydrostatic masses compared to the conservative combination of uncertainties in T_{CXO} and r_{500}^{WL} that was employed by I14.

2.3 Pseudo-XMM-Newton temperatures for the 400d clusters

The International Astronomical Consortium for High Energy Calibration (IACHEC) has tasked itself with improving (cross-)calibrations of X-ray satellite observatories (Grant et al. 2013). In this context, Schellenberger et al. (2014, S14) published a detailed comparison of *Chandra* and *XMM-Newton* temperatures for the HIFLUGCS sample of 64 high-flux local clusters, fitting spectra in the same radial and energy ranges. They not only confirmed earlier studies (e.g. Nevalainen, David & Guainazzi 2010) that *Chandra* yields significantly higher T_X than *XMM-Newton*, but also find significant differences between the *XMM-Newton* instruments. These temperature differences are most pronounced at the highest plasma temperatures and can best be explained as calibration uncertainties on effective area.

For the 400d cluster sample, we translate ICM temperatures measured with *Chandra*, T_{CXO} , to pseudo-*XMM-Newton* temperatures by applying the S14 conversion formula between ACIS and the combined *XMM-Newton* instruments for 0.7–7 keV energy range:

$$\log \left(\frac{k_B T_{\text{XMM}}}{1 \text{ keV}} \right) = A \cdot \log \left(\frac{k_B T_{\text{CXO}}}{1 \text{ keV}} \right) + B \quad (3)$$

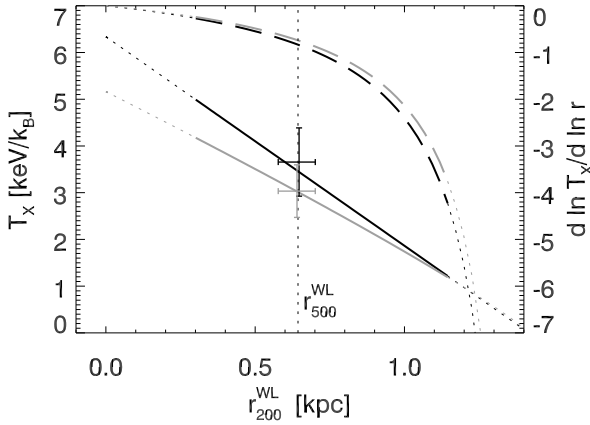


Figure 1. The effect of re-calibration on the temperature profile. The black solid line shows the Reiprich et al. (2013) *Chandra* temperature profile we assume for CL0030+2618. By applying Eq. (3), which is linear in $\log T_X$, to each datum of the profile, we derive the grey solid pseudo-*XMM-Newton* profile, which is slightly curved, but still close to the Reiprich et al. (2013) form. As indicated by the vertical line, r_{500} lies safely within the range (bold lines) in which the Reiprich et al. (2013) profile can be used. Long-dashed curves denote the logarithmic derivatives. For the sake of clarity, uncertainties are only shown at r_{500} .

Both the calibration of an X-ray instrument and our knowledge about it evolve with time. S14 assume calibrations as of December 2012 (*Chandra* Calibration Database v4.2), while V09a used the unchanged Vikhlinin et al. (2005) calibration procedure. This is no Calibration Database calibration, but at the time of observation v3.1 was in place. Therefore, we apply the following steps to derive pseudo-*XMM-Newton* temperature profiles:

1. We transform the V09a T_{CXO} from the energy range of 0.6–10 keV to 0.7–7 keV, by applying a correction

$$\log \left(\frac{k_B T_{\text{CXO}}^{(0.7-7)}}{1 \text{ keV}} \right) = A_0 \cdot \log \left(\frac{k_B T_{\text{CXO}}^{(0.6-10)}}{1 \text{ keV}} \right) + B_0 \quad (4)$$

with $A_0 = 1.0027 \pm 0.0018$ and $B_0 = -0.0008 \pm 0.0013$ derived from fitting the *Chandra* temperatures of the HIFLUGCS sample in the two spectral ranges, in analogy to S14. This raises the T_{CXO} values by 0.1 % to 0.3 %.

2. Using the timestamp correction for T_X between different Calibration Databases (Reese et al. 2010), derived for the 0.7–7 keV band, we convert the V09a temperatures to the one used by S14 (version 4.2). From Eq. (23) of Reese et al. (2010), we take a factor of $T_{\text{CXO},3.1}/T_{\text{CXO},4.2} = 1.06 \pm 0.05$.

3. For each of the 10^6 Monte Carlo realisations, we compute the *Chandra* temperature profile following Eq. (1). The black solid line in Fig. 1 shows an example (CL 0030+2618).

4. Finally, we perform the transformation (Eq. 3) between *Chandra* and the combined *XMM-Newton* instruments, in the 0.7–7 keV energy range. The best-fit parameters taken from S14 are $A = 0.889^{+0.005}_{-0.003}$ and $B = 0.000 \pm 0.004$. This transformation is applied to every datum of the temperature profile. As the grey solid line in Fig. 1 shows, the re-calibration introduces a slight curvature, because Eq. (3) is linear in $\log T_X$ rather than in T_X . Given the measurement uncertainties, the resulting departure from the form of Eq. (1) is insignificant.

By applying this conversion, we emulate what ICM temperatures would have been obtained for the *400d* clusters, had they been inferred from both the Metal Oxide Semiconductor (MOS) and the pn-CCD (PN) instruments (collectively, the *XMM-Newton European Photon Imaging Camera*, EPIC) instead of *Chandra*'s Advanced CCD Imaging Spectrometer (ACIS). We denote the resulting temperatures T_{xmm} , with the lowercase indicating that they are converted quantities, not actual *XMM-Newton* measurements.

For the eight I14 clusters, whose $\langle T_{\text{CXO}} \rangle = 4.4 \text{ keV}/k_B$ is representative of the full *400d* cosmology sample, we measure $\langle T_{\text{xmm}}/T_{\text{CXO}} \rangle = 0.81 \pm 0.01$, using the V09a cluster-averaged temperatures. At r_{500} , measured from weak lensing, the ratio is $\langle T_{\text{xmm}}/T_{\text{CXO}} \rangle = 0.85 \pm 0.01$. This ratio is closer to 1 because $T_X(r_{500}) < \langle T_X \rangle$ and the cross-calibration differences are smaller for lower T_X according to S14.

2.4 Pseudo-*XMM-Newton* hydrostatic masses

Within our Monte Carlo scheme, we re-derive hydrostatic masses by inserting the pseudo-*XMM-Newton* profiles $T_{\text{xmm}}(r)$ and their values at r_{500} into Eq. (2), thus accounting for the nonlinear nature of Eq. (3).

Differences in the effective area normalisation between *Chandra* and *XMM-Newton* also affect the measured gas mass M_{gas} and hydrostatic mass via the calibration of the flux S . As $M_{\text{gas}} \propto \sqrt{S}$, the 5 % flux difference for the full energy range in Nevalainen, David & Guainazzi (2010) correspond to 2 % uncertainty in M_{gas} . We account for this effect by rescaling the pseudo-*XMM-Newton* masses by 0.98.

As expected for lower input temperatures and flatter T_X gradients, we find the resulting pseudo-*XMM-Newton* hydrostatic masses for all clusters to be lower than the *Chandra*-measured values (Fig. 2). We point out that in Fig. 2, we do not apply the timestamp correction to the T_{CXO} , to highlight the combined effect of both corrections. The relative difference in masses is strongest for the hottest clusters, for which the S14 conversion results in the largest change. Because the I14 sample exhibits a limited T_X range of 3–6 keV, the relative change of the temperatures varies less than 5 %. Consequently, the two sets of hydrostatic masses are well fit by a linear relation (solid line in Fig. 2):

$$\frac{M_{500}^{\text{xmm}}}{10^{14} M_{\odot}} = P \cdot \frac{M_{500}^{\text{CXO}}}{10^{14} M_{\odot}} + Q \quad (5)$$

with $P = 0.783 \pm 0.007$ and $Q = 0.062 \pm 0.015$ that captures the dependence of the *Chandra*–*XMM-Newton* disagreement on the measured mass itself. As a sample average and standard error, we find $1 - b_{\text{lin}}^{\text{xcal}} = 1 - \langle M_{500}^{\text{xmm}}/M_{500}^{\text{CXO}} \rangle = 0.81 \pm 0.01$. The difference between this number and $1 - \langle T_{\text{xmm}}(r_{500}^{\text{wl}})/T_{\text{CXO}}(r_{500}^{\text{wl}}) \rangle = 0.15 \pm 0.01$ can be traced back to the additional factor of $T_X \left(\frac{d \ln T_X(r)}{d \ln r} \right)$ in Eq. (2).

2.5 Stronger WL mass bias for pseudo-*XMM-Newton* masses

Figure 3 shows the measured bias between the WL masses M_{500}^{wl} and M_{500}^{xmm} (including timestamp correction) for the I14 clusters. The bias is measured by averaging $\langle \log M^{\text{xmm}} - \log M^{\text{wl}} \rangle$ over the suite of Monte Carlo simulations described in Sect. 2.2 that was used to obtain the M_{500}^{xmm} measurements. The results are shown in Table 1 and indicated by a

Table 1. Observed mass bias in the I14 sample, for several choices of X-ray masses. Columns 2 and 3 give the slope P and intercept Q of the general best-fit relation (Eq. 5) between *Chandra* and *XMM-Newton* masses. Column 4 shows the X-ray calibration bias, i.e. the mean and standard error of $\langle M_{500}^{\text{xmm}} / M_{500}^{\text{CXO,I14}} \rangle$. Columns 5 and 6 show the apparent bias with respect to the *Chandra* masses, averaged over Monte Carlo simulations for all clusters ($b_{\log} = \langle \log M_{500}^{\text{xmm}} - \log M_{500}^{\text{CXO,I14}} \rangle$) and for the $M_{500}^{\text{wl}} \geq 10^{14.5} M_{\odot}$ bin ($b_{\log,H}$). The final column measures the mass-dependent mass bias as the difference $\Delta b_{\log}^{\text{H-L}}$ between b_{\log} for the high- and low-mass clusters.

Hydrostatic mass	P	Q	$b_{\text{lin}}^{\text{xc}}$	b_{\log}	$b_{\log,H}$	$\Delta b_{\log}^{\text{H-L}}$
M_{500}^{CXO} , new Monte Carlo	1	0	0	$0.02^{+0.10}_{-0.08}$	$-0.09^{+0.11}_{-0.10}$	$-0.20^{+0.20}_{-0.16}$
M_{500}^{CXO} , incl. timestamp correction	0.946 ± 0.009	-0.002 ± 0.020	0.06 ± 0.00	$-0.01^{+0.10}_{-0.09}$	-0.11 ± 0.11	$-0.20^{+0.20}_{-0.16}$
M_{500}^{xmm} , full conversion	0.783 ± 0.007	0.062 ± 0.015	0.19 ± 0.01	$-0.08^{+0.10}_{-0.08}$	$-0.19^{+0.11}_{-0.10}$	$-0.21^{+0.20}_{-0.16}$
M_{500}^{xmm} , temperature effects only	0.799 ± 0.007	0.064 ± 0.015	0.17 ± 0.01	$-0.07^{+0.10}_{-0.08}$	$-0.18^{+0.11}_{-0.10}$	$-0.21^{+0.20}_{-0.16}$
M_{500}^{xmm} , no timestamp correction	0.826 ± 0.004	0.061 ± 0.007	0.15 ± 0.01	$-0.05^{+0.10}_{-0.08}$	$-0.16^{+0.11}_{-0.10}$	$-0.21^{+0.20}_{-0.16}$

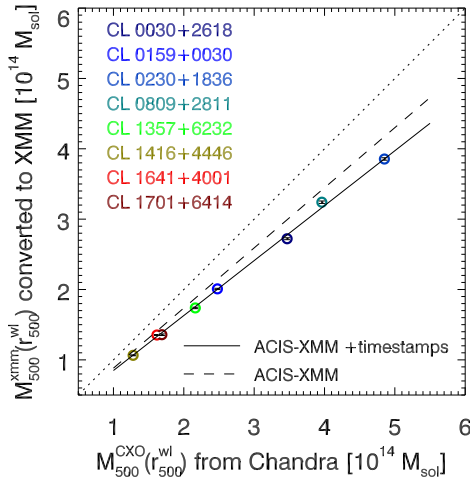


Figure 2. Mass estimates M_{500}^{xmm} derived from pseudo-*XMM-Newton* temperatures and assuming hydrostatic equilibrium as a function of masses M_{500}^{CXO} derived from ICM temperatures observed by *Chandra*. Error bars inscribed in the symbols denote the uncertainty in M_{500}^{xmm} due to the uncertainties in the ACIS-combined XMM and timestamp conversions. For illustrative purposes, the timestamp correction is not applied to the M_{500}^{CXO} , but its inverse to the M_{500}^{xmm} . The solid line marks the linear best fit. A dashed line marks the best-fit relation when the different *Chandra* calibration timestamps are not taken into account. For the latter case, data points are not shown for the sake of clarity.

dashed line and shading for the 1σ interval in Fig. 3. Dashed lines and boxes at $M_{500}^{\text{wl}} \leq 10^{14.5} M_{\odot}$ and $M_{500}^{\text{wl}} \geq 10^{14.5} M_{\odot}$ show the bias for the thus defined low- and high-mass sub-samples.

For the eight clusters, we now find a pronounced bias of $b_{\log} = -0.08^{+0.10}_{-0.08}$, compared to $b_{\log} = 0.02^{+0.10}_{-0.08}$ from *Chandra*, using the updated Monte Carlo method. For the low-mass sub-sample, M_{500}^{xmm} and M_{500}^{wl} are consistent ($b_{\log} = 0.02^{+0.16}_{-0.12}$); while for the high-mass sub-sample, we measure $b_{\log} = -0.19^{+0.11}_{-0.10}$, i.e. M_{500}^{xmm} that are smaller than WL masses by a similar amount as the M^{Pl} of vdL14 (cf. Fig. 3).

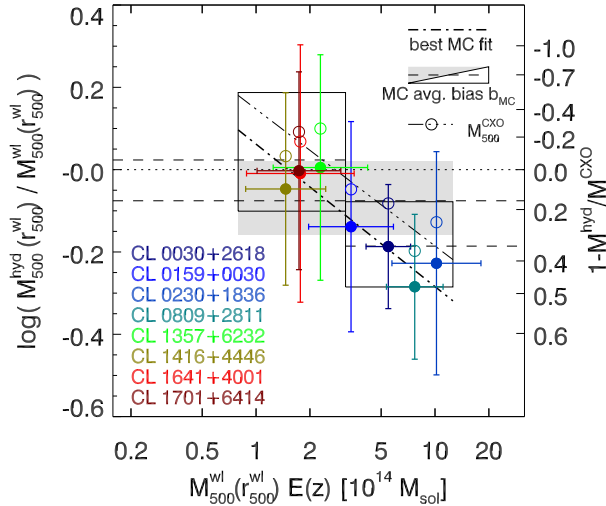


Figure 3. Ratio between the pseudo-*XMM-Newton* hydrostatic mass M_{500}^{xmm} , with timestamp correction, and the I14 WL mass M_{500}^{wl} as a function of M_{500}^{wl} . Short-dashed lines and light grey shading denote the logarithmic bias $b_{\log} = \langle \log M_{500}^{\text{xmm}} - \log M_{500}^{\text{wl}} \rangle$ obtained from averaging over Monte Carlo realisations. We also show b_{\log} for the low- M^{wl} and high- M^{wl} clusters separately, with the 1σ uncertainties presented as boxes, for sake of clarity. As a visual aid, a dot-dashed line depicts the Monte Carlo best-fit of $\log(M^{\text{xmm}}/M^{\text{wl}})$ as a function of M^{wl} . Empty symbols and the triple-dot-dashed line denote the M_{500}^{CXO} case. Compare to Fig. 2A in I14.

We repeat our analysis for a few modifications highlighting the relative importance of various contributing factors: First, we find that *Chandra* masses, converted to the newer CalDB v4.2 and the 0.7–7 keV band are systematically lower than for the V09a calibration and energy range. The *Chandra*-only timestamp calibration already accounts for $\sim 30\%$ of the difference with *XMM-Newton*: $b_{\log} = -0.01^{+0.10}_{-0.09}$, a difference of $\Delta b_{\log} = -0.03$ (Table 1). This result is consistent with the higher masses the V09a pipeline returns in the Rozo et al. (2014b,a) cross-calibration studies. Conversely, omitting the timestamps correction moves up the M_{500}^{xmm} , such that $b_{\log} = -0.05^{+0.10}_{-0.08}$ is less negative

by $\Delta b_{\log} = 0.03$. These comparisons demonstrate the importance of including the timestamp correction.

The 2 % difference the masses experience due to the different flux calibration of *Chandra* and *XMM-Newton* relates to a small, but measurable effect in the logarithmic bias: Ignoring it, we find a slightly milder bias of $b_{\log} = -0.07^{+0.10}_{-0.08}$ compared to the full conversion ($b_{\log} = -0.08^{+0.10}_{-0.08}$).

Considering the full mass range, the *XMM-Newton* hydrostatic masses are ~ 20 % lower than the WL masses, while *Chandra* masses are consistent with the WL masses. This indicates that if the $b_{\text{lin}} = 0.2$ linear hydrostatic bias in cluster simulations is correct, the effective area calibration of *XMM-Newton* is consistent with being correct. But if looking at the high mass end, the conclusion is the opposite: *Chandra* is consistent with the correct calibration and 20 % hydro bias. The measurement uncertainties and the unknown amount of Eddington bias in our small sample, however, preclude more quantitative conclusions.

2.6 Mass-dependent bias with *XMM-Newton*

Finally, we measure the mass-dependence of the bias as the difference $\Delta b_{\log}^{\text{H-L}}$ between the logarithmic biases b_{\log} for the high- and low-mass clusters. This observable is stable against changes to the details of the probability distribution modelling in the Monte Carlo algorithm. (Note that fitting $\log(M^{\text{xmm}}/M^{\text{wl}})$ as a function of M^{wl} is not stable.)

In I14, the hydrostatic mass exhibited the least significant mass-dependent bias of four tested mass observables. For the four more massive clusters, b_{\log} is $\sim 1\sigma$ different to the four less massive ones, as opposed to $\sim 2\sigma$. We reproduce this result and measure $\Delta b_{\log}^{\text{H-L}} = -0.20^{+0.20}_{-0.16}$ for *Chandra* and $\Delta b_{\log}^{\text{H-L}} = -0.21^{+0.20}_{-0.16}$ for *XMM-Newton* (Table 1).

We interpret the observed mass-dependence of b_{\log} as the superposition of 1.) physical effects, e.g. the stronger hydrostatic bias for high-mass clusters Shi & Komatsu (2014) predict analytically, and 2.) Eddington bias: As Sereno & Ettori (2014) demonstrate, intrinsic scatter in the abscissa mass leads to a mass-dependent bias when compared to an independent mass observable. Eddington bias is most severe in our case of a small sample size and a narrow range in the underlying true mass. In principle, the statistically complete nature of the 400d cosmology (V09a) sample would allow for a rigorous correction of such selection effects, once the WL follow-up has been completed. For our given subsample, the Eddington bias and true mass-dependent mass bias cannot be disentangled. While we can provide much needed *relative* cross-calibrations between X-ray and WL instruments/pipelines, selection effects preclude us from determining absolute calibrations for *Chandra* and *XMM-Newton*. Moreover, selection biases also limit the direct applicability of $\Delta b_{\log}^{\text{H-L}}$ to other cluster samples.

3 TRANSLATION TO PLANCK CLUSTERS

3.1 What did the *Planck* collaboration measure?

P13XX model the redshift-dependent abundance of clusters detected from the *Planck* catalogue of Sunyaev-Zeldovich sources (Planck Collaboration et al. 2013a, P13XXIX), covering the whole extragalactic sky. The thermal SZ effect

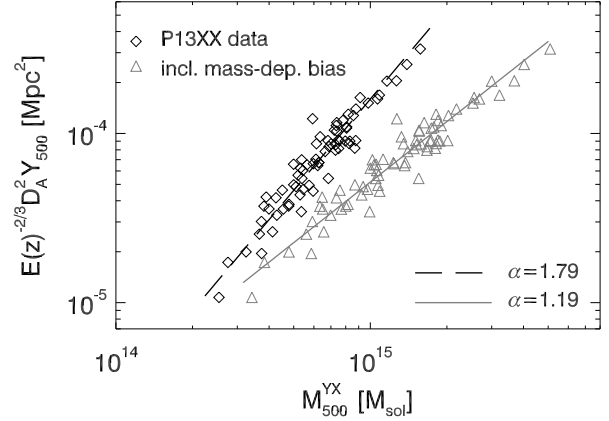


Figure 4. The P13XX calibration sample. Diamonds and the long-dashed fit line show the SZ signal as a function of original P13XX Y_X mass (compare their Fig. A.1). Triangles and the solid fit line show rescaled masses, assuming an extreme case of a mass-dependent hydrostatic bias.

describes the inverse Compton scattering of CMB photons with ICM electrons, resulting in a distortion Y_{SZ} of the CMB signal in the solid angle subtended by a galaxy cluster, proportional to the integrated electron pressure. All 189 $S/N > 7$ sources selected from the P13XXIX catalogue are confirmed clusters of known redshift; the vast majority with spectroscopic redshifts. The P13XXIX mass estimates M^{Pl} (M^{Y_z} in P13XXIX) that enter the P13XX calculation are the only, and crucial, piece of *Planck* data P13XX use.

Due to the large beam compared to the typical *Planck* cluster size, the aperture size θ , in which Y_{SZ} is integrated, is hard to determine from the SZ data itself. P13XXIX rely on the additional $Y_{\text{SZ}}(\theta)$ constraint provided by the scaling of Y_{SZ} with an X-ray mass proxy, $M_{500}^{Y_X}$, to fix θ and calibrate the M^{Pl} . By convention, r_{Δ} denotes a radius such that the mass M_{Δ} within it exceeds the critical density $\rho_c(z)$ at redshift z by a factor of Δ . The $M_{500}^{Y_X}$ mass proxy is based on $Y_X = T_X M_{\text{gas}}$, which is the product of the ICM temperature T_X and the cluster gas mass M_{gas} , measured from X-rays within r_{500} , and thus provides an X-ray analogue of Y_{SZ} .

P13XX calibrate M^{Pl} on a validation sub-sample of 71 clusters observed with *XMM-Newton*, i.e. they derive the best-fit $Y_{\text{SZ},500} - M_{500}^{Y_X}$ relation. In turn, $M_{500}^{Y_X}$ was calibrated on a sample of 500 local, relaxed clusters whose “true” masses could be measured using X-ray observations and assuming hydrostatic equilibrium (Arnaud et al. 2010). All EPIC instruments were used, with the pn/MOS normalisation as a free parameter. Spectra were fitted in the 0.3–10 keV energy band (M. Arnaud; priv. comm.). It is via this ladder of mass proxies that the hydrostatic mass bias is inherited onto M^{Pl} , appearing in the $Y_{\text{SZ},500} - M_{500}^{Y_X}$ relation that summarises the calibration process (Eq. A.8 of P13XX). P13XX considered a flat prior of $0.7 < (1 - b_{\text{lin}}) < 1$, but any additional systematic effect in the calibration chain would mimic a spurious “hydrostatic” bias.

3.2 Comparison to *Planck* and vdL14 samples

The mean WL mass of the I14 high-mass sub-sample is $4.9 \cdot 10^{14} M_{\odot}$. The typical P13XX cluster mass, defined by

their mass pivot $\sim 6 \cdot 10^{14} M_\odot$, falls into the mass range probed by the I14 high- M^{wl} range, even although the mass bias is not included. Therefore, for the relevant P13XX mass range, our result of $b_{\log, H} = 0.20^{+0.17}_{-0.16}$ agrees with the $1 - b_{\text{lin}} \approx 0.4$ that would reconcile cosmological constraints derived from *Planck* cluster counts (P13XX) and primary CMB anisotropies (P13XVI).

The high-mass end of the I14 sample also overlaps with the vdL14 sample. Using the M_{500}^{XMM} for the I14 clusters instead of *Chandra* masses, we also find better agreement to the vdL14 measurement of $\langle M^{\text{P1}}/M^{\text{wl}} \rangle = 0.688 \pm 0.072$ for a subset of P13XX clusters. However, such comparisons are limited by the small number statistics of our sample, hence caution is necessary when interpreting these results.¹

Complications arise from the different energy range used for *Planck* and the temporal variability of X-ray calibrations. Our results for the cases with and without time-stamp correction (Table 1) tell us, however, that the impact of those systematics is rather small, with $\Delta b_{\text{lin}} \lesssim 0.05$.

3.3 How much can X-ray calibration bias have influenced the P13XX results?

3.3.1 From *Planck* pre-calibration to calibration

We attempt to estimate how an additional bias $b_{\text{lin}}^{\text{Xcal}}$ arising from the *XMM-Newton* calibration relative to *Chandra* will influence the overall bias measured by P13XX. We emphasise that we do not know or assume which, if any, satellite calibration is correct. The “pre-calibration” from 20 relaxed clusters (Arnaud et al. 2010) determines the normalisation 10^B and slope β of a scaling relation

$$E^{-2/3}(z) \left[\frac{Y_X}{2 \cdot 10^{14} M_\odot \text{ keV}} \right] = 10^B \cdot \left[\frac{M_{500}^{\text{HE}}}{6 \cdot 10^{14} M_\odot} \right]^\beta \quad (6)$$

between the Y_X and hydrostatic masses M_{500}^{HE} measured with *XMM-Newton*. The evolution factor $E(z) = H(z)/H(z=0)$ depends on cosmology via the Hubble parameter $H(z)$.

In Eq. (6), M_{500}^{HE} scales roughly as $T_X^{3/2}$ (e.g., Kay et al. 2012), through the measurement at r_{500} . If $q = T_{\text{XMM}}/T_{\text{CXO}}$ for the typical Arnaud et al. (2010) cluster, hydrostatic masses are biased $M_{500}^{\text{HE}} \rightarrow q^\delta M_{500}^{\text{HE}}$, with $\delta \approx 1.5$. Similarly, Y_X depends on T_X via the measurement of the gas mass M_{gas} within r_{500} : We have $r_{500} \propto M_{500}^{1/3}$. If $M_{500} \propto T_X^{3/2}$ upon a change in T_X , then $r_{500} \propto (T_X^{3/2})^{1/3} = T_X^{1/2}$. Because $M_{\text{gas}}(< r)$ increases linearly with r in a given cluster² it follows $M_{\text{gas}, 500} \propto T_X^{1/2}$ upon a change in T_X . Indeed, we measure $M_{\text{gas}, 500}$ to be affected as $q^{0.5-0.6}$ to by a relative temperature change q , using the V09a gas density model for the I14 clusters. Hence, we have $Y_X \rightarrow q^\gamma Y_X$ with an exponent $\gamma \approx 1.5$. Thus T_X re-calibration affects Eq. (6) like:

¹ The difference in cosmologies between P13XX and vdL14 on the one hand (flat universe with matter density $\Omega_m = 0.3$ and Hubble parameter $H_0 = 70 \text{ km s}^{-1} \text{ Mpc}^{-1}$) and I14 and this work the other hand (the same, but $H_0 = 72 \text{ km s}^{-1} \text{ Mpc}^{-1}$) adds a factor of 70/72 to convert *Planck* masses to our cosmology.

² If the cluster is isothermal, and $\rho_{\text{gas}} \propto r^{-2}$, as motivated by assuming the standard $\beta = 2/3$ in the β model for the gas density (Cavaliere & Fusco-Femiano 1978), then the 3D mass within a radius R is $M(< R) = \int_0^R \rho_{\text{gas}}(r) dV \propto \int_0^R r^{-2} r^2 dr = R$.

$$q^\gamma Y_X \propto [q^\delta M_{500}^{\text{HE}}]^\beta \Leftrightarrow Y_X \propto q^{\beta\delta-\gamma} [M_{500}^{\text{HE}}]^\beta. \quad (7)$$

For a (residual, unaccounted) temperature bias q , the mass proxy $M_{500}^{Y_X}$ will be biased by a factor $C = q^{\beta\delta-\gamma}$. This factor propagates into the main P13XX scaling relation, connecting the masses $M_{500}^{Y_X}$ to Y_{500} instead of Y_X :

$$E^{-2/3}(z) \left[\frac{D_A^2 Y_{\text{SZ}, 500}}{10^{-4} \text{ Mpc}^2} \right] = 10^A q^{\alpha\delta-\gamma} \cdot \left[\frac{M_{500}^{Y_X}}{6 \cdot 10^{14} M_\odot} \right]^\alpha \quad (8)$$

Here, D_A denotes the angular diameter distance. Because Y_X is theoretically expected to be proportional to Y_{SZ} , we identified $\alpha = \beta$ in Eq. (8).

3.3.2 Results for temperature re-calibration

The Arnaud et al. (2010) clusters used in the *Planck* pre-calibration show an average $^3 k_B T_{\text{XMM}} \approx 5 \pm 2 \text{ keV}$ (Arnaud, Pointecouteau & Pratt 2007; Pratt et al. 2010). Following Eq. (3), the S14 conversion for the combined *XMM-Newton* instruments, *Chandra* temperatures for these clusters would be lower by a factor of $q = 0.84^{+0.05}_{-0.03}$.

Using $\alpha = 1.79 \pm 0.06$ from P13XX, and $\gamma = 1.5 \pm 0.3$ and $\delta = 1.5 \pm 0.3$ (i.e. allowing for broad uncertainties in both), we find the normalisation of Eq. (8) to be reduced by a factor of $C = 0.81 \pm 0.09$.

3.3.3 Breaking the size-flux degeneracy

The exact algorithm by which P13XXIX combine *Planck* measurements with Eq. (8) has yet to be published. However, using $\theta_{500} = (3M_{500}/[4\pi\rho_c D_A^3])^{1/3}$, one can easily convert Eq. (8) into a scaling relation in terms of an aperture scale θ_{500} , i.e.: $Y_{\text{SZ}} \propto \theta_{500}^{3\alpha}$. The intersection of this relation with the size-flux degeneracy modelled as $Y_{\text{SZ}}^{\text{obs}} \propto \theta^\lambda$ yields a point (θ_X, Y_X) , that can in turn be used to compute an SZ mass $M_{\text{P1}} \propto \theta_X^3$. Thus, the degeneracy is broken. How is this M_{P1} affected if the normalisation of Eq. (8) changes by a factor C ? We geometrically infer the changes in the intersection point and final mass as:

$$\log(Y'_X/Y_X) = [-\lambda/(\lambda-3\alpha)] \cdot \log C \quad (9)$$

$$\log C_{\text{fin}} = \log(M'_{\text{P1}}/M_{\text{P1}}) = [-3\alpha\lambda/(\lambda-3\alpha)] \cdot \log C. \quad (10)$$

From Fig. 4 of P13XXIX, we read that the $Y_{\text{SZ}}^{\text{obs}} - \theta$ relation is linear, so $\lambda = 1$. With $C = 0.81^{+0.05}_{-0.03}$ from above, we find that cluster masses would be biased low by a factor $C_{\text{fin}} = 0.78^{+0.10}_{-0.07}$ due to the temperature calibration. Thus, if the *Chandra* calibration was correct, the need for a hydrostatic mass bias of more than the $\sim 20\%$ favoured by simulations would be eased. Alternatively, if the *XMM-Newton* calibration was correct, evidence for stronger departures from hydrostatic equilibrium would persist.

We note that the “hydrostatic” bias b_{lin} that P13XX consider is meant to include instrumental calibration effects: $1 - b_{\text{lin}} = (1 - b_{\text{lin}}^{\text{hyd}})(1 - b_{\text{lin}}^{\text{Xcal}}) \approx (1 - b_{\text{lin}}^{\text{hyd}} - b_{\text{lin}}^{\text{Xcal}})$. Nevertheless even a partially unaccounted calibration bias would contribute some of the apparent mass discrepancy. The point of this exercise lies not in suggesting that the *Planck* discrepancy

³ In principle, the temperature recalibration should be applied to individual clusters. This would alter the slope β in Eq. (6) in a similar way as the mass-dependent mass bias discussed below.

is caused by the X-ray calibration. Rather it should serve to demonstrate how such effects can not only fold through but even become amplified in a multi-step calibration.

3.3.4 Inclusion of the mass-dependent bias

The above calculations treat the case of a potential residual temperature calibration offset in the *Planck* calibration. To this end, we assume the hydrostatic mass bias to be taken into account and well represented by the P13XX baseline value of $(1 - b_{\text{hyd}}) = 0.8^{+0.2}_{-0.1}$.

But it is instructive to include a mass-dependent hydrostatic mass bias, as suggested by I14 and Fig. 3. Because we are interested in extreme cases, we assume that the best-fit $b_{\log}(M_{500}^{\text{xmm}}) = -0.346 \cdot (E(z)M_{500}^{\text{xmm}}/2.44 \cdot 10^{14} M_{\odot}) - 0.111$ is purely physical (departure from hydrostatic equilibrium). We emphasise this is not the case: As detailed in Sect. 2.6, not all of the mass-dependence is physical, but an unknown fraction is caused by selection effects (Eddington bias).

Figure 4 shows how a mass-dependent mass bias differentially stretches the mass range occupied by the *Planck* calibration clusters. In our extreme scenario, masses for all clusters are higher after accounting for b_{\log} (triangles) than before (diamonds), but most so for the most massive ones. Consequently the slope of Eq. (8) needs to be corrected from P13XX's $\alpha = 1.79 \pm 0.06$ to a lower value of $\alpha = 1.19 \pm 0.04$.⁴

Interestingly, a flatter $Y-M$ slope largely cancels out the temperature re-calibration effect seen in Sect. 3.3.3. With $\alpha = 1.19 \pm 0.04$, we arrive at a factor of $C = 0.95^{+0.08}_{-0.05}$ in Eqs. (8) and final *Planck* masses different by a factor of $C_{\text{fin}} = 0.94^{+0.11}_{-0.07}$. We conclude that inclusion of a mass-dependent hydrostatic bias that grows more negative with mass cannot increase the final calibration offset. The better, still partial, alleviation of the *Planck* cluster counts–CMB discrepancy is achieved from X-ray calibration effects alone.

4 SUMMARY AND OUTLOOK

Starting from the recent Schellenberger et al. (2014) comparative study of ICM temperatures measured with *Chandra* and *XMM-Newton*, we revisit the bias between WL and hydrostatic masses from Israel et al. (2014). We find:

1. Because of different uncertainties in the effective area calibration, hydrostatic masses for the I14 clusters would have been measured to be ~ 15 – 20 % lower, had the clusters been observed with *XMM-Newton* instead of *Chandra*. The measured calibration bias depends on the sample, but can be transferred to clusters of similar mass (10^{14} – $10^{15} M_{\odot}$).
2. *XMM-Newton* masses for the most massive I14 clusters are lower than WL masses by ~ 35 %.
3. Assuming a true hydrostatic bias of $b_{\text{lin}}^{\text{hyd}} = 0.2$, our results for the whole mass range indicate that the calibration of the energy dependence of the effective area of the *XMM-Newton* EPIC instruments in the 0.6–10.0 keV band is rather

accurate. In the high mass range the data however indicate that *Chandra* calibration is more accurate. Given the uncertainties these results are not significant.

In addition, we consider the *Planck* clusters and find:

4. Hence, consistent with vdL14, a bias of $(1 - b_{\text{lin}}^{\text{hyd}} - b_{\text{lin}}^{\text{xcal}}) \approx 0.4$ for the rather massive P13XX clusters seems plausible.
5. If there was a residual calibration bias q in the T_{XMM} measurements on which the *Planck* analysis is based, the normalisation of the P13XX $Y_{\text{SZ}} - M^{\text{Xx}}$ calibration would be affected as $C = q^{\sim 1.2}$. We show that the mass bias further amplifies when propagated into the SZ masses. Without accounting for calibration uncertainties, a mass bias of up to 20 % is plausible. We do not claim that this is the case for *Planck*. However, a small, residual bias would amplify in the same way. Pointing to the S14 result that calibration alone cannot explain the discrepant cosmological parameters of P13XVI and P13XXIX, we conclude that a possible contribution would ease the discrepancy and allow for a true hydrostatic bias consistent with simulations.
6. A hydrostatic bias increasing with mass counteracts the amplification of a calibration bias.

Our results are consistent with the WL/X-ray mass biases recently reported by Donahue et al. (2014), comparing CLASH WL mass profiles to those obtained with *Chandra* and *XMM-Newton*. Donahue et al. (2014) found their $T_{\text{XMM}}/T_{\text{CXO}}$ and $M^{\text{XMM}}/M^{\text{WL}}$ to depend on the integration radius; suggesting soft X-ray scattering as a cause for the calibration offset. Donahue et al. (2014) study mostly cool core clusters. Since S14 find that the T_{X} bias depends on T_{X} , this could explain why they find less bias in the cooler centres. The radial dependence could at least partly be due to a secondary correlation: at the radius where the cluster temperature is typically hottest, the largest discrepancy between *Chandra* and *XMM-Newton* is found.

Cluster mass calibrations still bear considerable uncertainties not only between the main techniques (X-ray, lensing, SZ, galaxy-based), but also within techniques, i.e. for different instruments and calibration and methods. Thorough cross-calibration of different instruments and techniques, as already performed by Nevalainen, David & Guainazzi (2010); Schellenberger et al. (2014); Rozo et al. (2014b,a) for X-rays are the necessary way forward. Recent comparisons of WL masses to both *XMM-Newton* and *Chandra* include Mahdavi et al. (2013); Donahue et al. (2014), and Martino et al. (2014). We notice that Martino et al. (2014) find temperature discrepancies between *XMM-Newton* and *Chandra* similar to S14, but consistent hydrostatic masses from both satellites. More overlap between clusters with X-ray and WL data would be necessary to define mass standards against which other surveys could then be gauged.

Recently, Sereno & Ettori (2014); Sereno, Ettori & Moscardini (2014) compared several of the larger current WL and *XMM-Newton* and *Chandra* X-ray samples, emphasising how intrinsic and measurement scatter can induce scaling relation biases. Sereno & Ettori (2014) confirm that compared to simulated clusters WL masses are biased low by ~ 10 % and hydrostatic masses by ~ 20 – 30 %. However, these authors find literature masses from the same observable, X-ray or WL, can differ up to 40 % for the same cluster, impeding an absolute calibration. Sereno, Ettori &

⁴ Observations of the $Y-M$ relation have yet to reach an accuracy that would constrain the mass-dependency of the hydrostatic bias. While Bender et al. (2014) and Czapon et al. (2014) report low best-fit $Y-M$ slopes consistent with $\alpha \approx 1.2$, Liu et al. (2014) find a slope steeper than the self-similar value of 5/3.

Moscardini (2014) extend the analysis to the *Planck* clusters, whose absolute mass calibration is likewise affected. They find scatter in the calibration scaling relation to invoke a mass-dependent bias in the *Planck* masses.

Here, the *400d* cluster sample provides *relative* calibrations between the different instruments and methods. Once the WL follow-up has been completed, we will be able to disentangle the physical mass-dependent mass bias from selection effects, and provide *absolute* calibrations.

The advent of larger SZ samples for scaling relation studies (e.g., Bender et al. 2014; Czakon et al. 2014; Liu et al. 2014), and foremost the all-sky P13XXIX offers the possibility to include a complementary probe and clusters at higher redshift. For future high precision cluster experiments, e.g., *eROSITA* (Predehl et al. 2010; Merloni et al. 2012; Pillepich, Porciani & Reiprich 2012) or *Euclid* (Lauzeijs et al. 2011; Amendola et al. 2012) the absolute X-ray observable–mass calibration needs to be improved further.

REFERENCES

- Amendola L. et al., 2012, ArXiv astro-ph.CO/1206.1225
 Applegate D. E. et al., 2014, MNRAS, 439, 48
 Arnaud M., Pointecouteau E., Pratt G. W., 2007, A&A, 474, L37
 Arnaud M., Pratt G. W., Piffaretti R., Böhringer H., Croston J. H., Pointecouteau E., 2010, A&A, 517, A92
 Battye R. A., Moss A., 2014, Physical Review Letters, 112, 051303
 Bender A. N. et al., 2014, ArXiv astro-ph.CO/1404.7103
 Bhattacharya S., Habib S., Heitmann K., Vikhlinin A., 2013, ApJ, 766, 32
 Burenin R. A., Vikhlinin A., Hornstrup A., Ebeling H., Quintana H., Mescheryakov A., 2007, ApJS, 172, 561
 Cavaliere A., Fusco-Femiano R., 1978, A&A, 70, 677
 Costanzi M., Sartoris B., Viel M., Borgani S., 2014, ArXiv astro-ph.CO/1407.8338
 Czakon N. G. et al., 2014, ArXiv astro-ph.CO/1406.2800
 Donahue M. et al., 2014, ArXiv astro-ph.CO/1405.7876
 Grant C. E., Guainazzi M., Natalucci L., Nevalainen J., Plucinsky P. P., Pollock A., Sembay S., 2013, ArXiv astro-ph.IM/1305.4480
 Hamann J., Hasenkamp J., 2013, JCAP, 10, 44
 Israel H. et al., 2010, A&A, 520, A58
 Israel H., Erben T., Reiprich T. H., Vikhlinin A., Sarazin C. L., Schneider P., 2012, A&A, 546, A79
 Israel H., Reiprich T. H., Erben T., Massey R. J., Sarazin C. L., Schneider P., Vikhlinin A., 2014, A&A, 564, A129
 Kay S. T., Peel M. W., Short C. J., Thomas P. A., Young O. E., Battye R. A., Liddle A. R., Pearce F. R., 2012, MNRAS, 422, 1999
 Kelly P. L. et al., 2014, MNRAS, 439, 28
 Laganá T. F., de Souza R. S., Keller G. R., 2010, A&A, 510, A76
 Laureijs R. et al., 2011, ArXiv astro-ph.CO/1110.3193
 Le Brun A. M. C., McCarthy I. G., Schaye J., Ponman T. J., 2014, MNRAS, 441, 1270
 Liu J. et al., 2014, ArXiv astro-ph.CO/1407.7520
 Mahdavi A., Hoekstra H., Babul A., Bildfell C., Jeltama T., Henry J. P., 2013, ApJ, 767, 116
 Mantz A. B. et al., 2014, ArXiv astro-ph.CO/1407.4516
 Martino R., Mazzotta P., Bourdin H., Smith G. P., Bartalucci I., Marrone D. P., Finoguenov A., Okabe N., 2014, ArXiv astro-ph.CO/1406.6831
 Merloni A. et al., 2012, ArXiv astro-ph.HE/1209.3114
 Nagai D., Kravtsov A. V., Vikhlinin A., 2007, ApJ, 668, 1
 Nevalainen J., David L., Guainazzi M., 2010, A&A, 523, A22
 Pillepich A., Porciani C., Reiprich T. H., 2012, MNRAS, 422, 44
 Planck Collaboration et al., 2013a, ArXiv astro-ph.CO/1303.5089
 Planck Collaboration et al., 2013b, ArXiv astro-ph.CO/1303.5076
 Planck Collaboration et al., 2013c, ArXiv astro-ph.CO/1303.5080
 Pratt G. W. et al., 2010, A&A, 511, A85
 Predehl P. et al., 2010, in Society of Photo-Optical Instrumentation Engineers (SPIE) Conference Series, Vol. 7732
 Rasia E. et al., 2012, New Journal of Physics, 14, 055018
 Reese E. D., Kawahara H., Kitayama T., Ota N., Sasaki S., Suto Y., 2010, ApJ, 721, 653
 Reiprich T. H., Basu K., Ettori S., Israel H., Lovisari L., Molendi S., Pointecouteau E., Roncarelli M., 2013, Space Sci. Rev., 195
 Rozo E., Evrard A. E., Rykoff E. S., Bartlett J. G., 2014a, MNRAS, 438, 62
 Rozo E., Rykoff E. S., Bartlett J. G., Evrard A., 2014b, MNRAS, 438, 49
 Schaye J. et al., 2014, ArXiv astro-ph.GA/1407.7040
 Schellenberger G., Reiprich T. H., Lovisari L., Nevalainen J., David L., 2014, ArXiv astro-ph.IM/1404.7130
 Sereno M., Ettori S., 2014, ArXiv astro-ph.CO/1407.7868
 Sereno M., Ettori S., Moscardini L., 2014, ArXiv astro-ph.CO/1407.7869
 Shi X., Komatsu E., 2014, MNRAS, 442, 521
 Vikhlinin A. et al., 2009a, ApJ, 692, 1033
 Vikhlinin A., Kravtsov A., Forman W., Jones C., Markevitch M., Murray S. S., Van Speybroeck L., 2006, ApJ, 640, 691
 Vikhlinin A. et al., 2009b, ApJ, 692, 1060
 Vikhlinin A., Markevitch M., Murray S. S., Jones C., Forman W., Van Speybroeck L., 2005, ApJ, 628, 655
 von der Linden A. et al., 2014a, MNRAS, 439, 2
 von der Linden A. et al., 2014b, MNRAS, 443, 1973

ACKNOWLEDGEMENTS

We thank the the *Planck* collaboration for making available the calibration sample in the SZ cluster database (<http://szcluster-db.ias.u-psud.fr>). We thank the referee for helpful comments. HI would like to thank D. Applegate for a helpful discussion. HI acknowledges support from European Research Council grant MIRG-CT-208994 and Philip Leverhulme Prize PLP-2011-003. JN acknowledges a PUT 246 grant from Estonian Research Council. RJM is supported by a Royal Society University Research Fellowship. THR acknowledges support from the German Research Association (DFG) through Heisenberg grant RE 1462/5 and through the Transregional Collaborative Research Centre TRR33 “The Dark Universe” (project B18). GS and THR acknowledge DFG grant RE 1462/6.